Preliminary MITR Design-Demonstration Element Thermal-Hydraulics and Structural Analyses

October 2022

Mauricio E. Tano
SuJong Yoon

Idaho National Laboratory

Preliminary MITR Design-Demonstration Element Thermal-Hydraulics and Structural Analyses

Mauricio E. Tano
SuJong Yoon

October 2022

Page intentionally left blank

CONTENTS

FIGURES

TABLES

ACRONYMS

AGR	Advanced Gas Reactor
ARIS	Advanced Reactors Information System
ARTIST	Advanced Reactor Technology Integral System Test
ASME	American Society of Mechanical Engineers
BANR	BWXT Advanced Nuclear Reactor
CBC	Closed Brayton cycle
DOD	Department of Defense
DOE	Department of Energy
FERC	Federal Energy Regulatory Commission
HALEU	High Assay Low-Enriched Uranium
HTGR	High-temperature gas reactor
IAEA	International Atomic Energy Agency
IHX	Intermediate Heat Exchanger
INL	Idaho National Laboratory
ITAAC	Inspections, Tests, Analyses, and Acceptance Criteria
MAGNET	Microreactor Agile Non-Nuclear Experimental Test
MMR	Micro Modular Reactor
MW	Mega Watts
NGTCC	Nuclear gas turbine combined cycle power plant concept
NIST	National Institute of Standards and Technology
NRC	Nuclear Regulatory Commission
PCHE	Printed circuit heat exchanger
SFR	Sodium fast reactor
SPM	Subcritical power modules
TRISO	tristructural isotropic
TRL	Technology Readiness Level
TRUST	Thermal-hydraulic Research Universal Scoping Tool
VHTR	Very-high temperature reactors

Page intentionally left blank

MITR

1. INTRODUCTION

1.1 OBJECTIVE

The United State High Performance Research Reactor (USHPRR) program aims to eliminate more than 200kg of High Enriched Uranium (HEU) from commerce annually by converting five U.S. high-performance research reactors and one associated critical assembly to Low Enriched Uranium (LEU) fuel using a high-density alloy of uranium-10 wt% molybdenum (U-10Mo). Massachusetts Institute of Technology Reactor (MITR) is one of five research reactors selected for this program. The objective of this report is to provide preliminary thermal-hydraulic and mechanical analyses of the hydrodynamic effects in the MITR Design Demonstration Element (DDE) under conservative approximations for the plate power distribution. This report provides details on the modeling approach and the simulation results obtained, including pressure, flow velocity, temperature, and oxide layer over the design demonstration experiment for the irradiation cycles in the Belgian Reactor (BR)-2.

2. PROBLEM DESCRIPTION

The current section describes the geometry, boundary conditions, and material properties used for the analyses of the MITR DDE.

2.1   MITR GEOMETRY

The CAD-based geometry provided by SCK CEN and dimensions of MITR DDE are depicted in Figure 1 and Figure 2 The MITR DDE consists of a top coupling basket, bottom coupling basket, and the DDE basket which contains the fuel assembly. The upper part of Figure 1 shows the three components assembled. The length of fuel plate is 23 inches. There are three types of plate that have different thickness of fuel core as depicted in Figure 2. Plates #1 and #19 employ Type-T fuel core with 0.013-inch thickness, plates #2, #3, #17, and #18 employ Type-Y fuel core with 0.017-inch thickness, and plates #4-16 employ Type-F fuel core with 0.025-inch thickness. The width and length of fuel core in this ECAR are 2.166 inches and 22.75 inches, respectively.
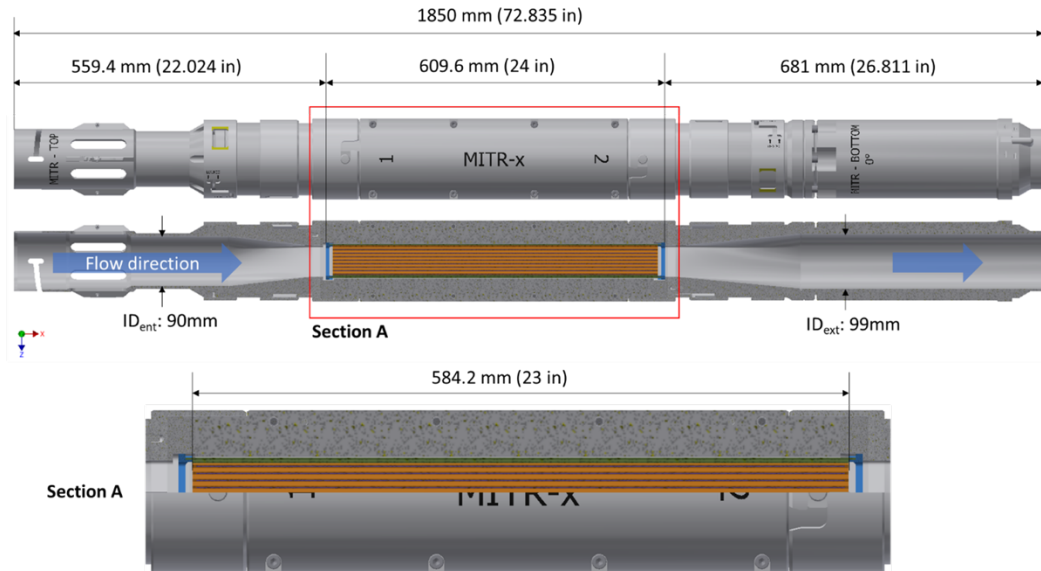

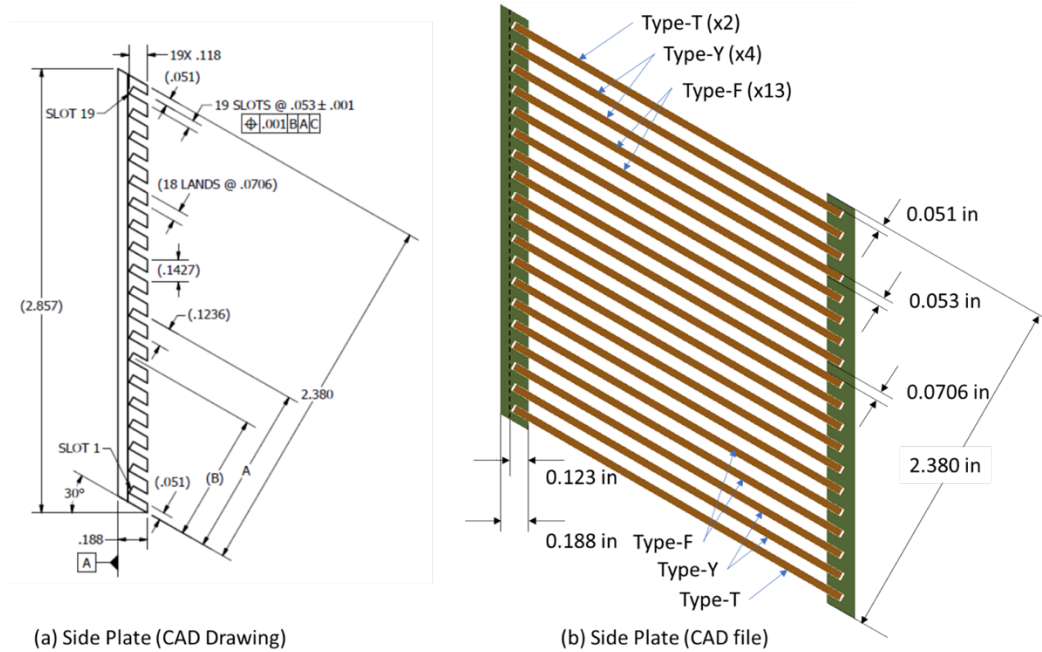Figure 1. MITR DDE basket and fuel assembly.

Figure 2. MITR DDE fuel assembly plates.

2.2 BOUNDARY CONDITIONS

The power density distributions of MITR DDE during the first and second irradiation campaigns have been provided from SCK CEN [Kalcheva, 2022] and are presented in Table 1. There are 8 irradiation cycles and the power density at each Beginning of Cycle (BOC) is provided. The power density provided for plate #16 is used for plates #1 through #16, the power density provided for plate #18 is used for the plates #17 and #18, and the power density provided for plate #19 is only used for plate #19. There are four transverse regions in MITR DDE fuel core, which are captured only in the CFD model. However, the value Table 1was used for all four transverse regions. Moreover, the axial distribution of power density is assumed to be uniform for each plate. The power distribution assumed is conservative in the sense that, for every position over the pate, the actual plates power should be smaller or equal to the one assumed in this modeling approach.

Table 1. Power Density calculated and assumed in MITR DDE fuel plates during the irradiation campaigns, the cycle time of each cycle was 31.5 days and the power during each irradiation campaign is assumed constant and equal to the Beginning of Cycle (BOC) power.

Irradiation Campaign	MITR-Al-basket & Al-plug (12 Hf-rods)		
	Power Density (kW/cm^3)		
	Power Modeled for Plate	1-16	17-18	19
	Actual Plate for Power Reference	16	18	19
1st standalone irradiation of MITR-DDE in position H5	BOC 1, Power = 55 MW	1.87	2.77	3.8
	BOC 2, Power = 56 MW	1.84	2.66	3.62
	BOC 3, Power = 56 MW	1.84	2.71	3.57

	BOC 4, Power = 56 MW	1.83	2.69	3.52
	BOC 5, Power = 56 MW	1.83	2.58	3.23
2nd simultaneous irradiation of MITR-DDE in position H5 and NBSR-DDE in position H3	BOC 6, Power = 56 MW	2.94	3.90	4.55
	BOC 7, Power = 56 MW	2.95	3.65	4.34
	BOC 8, Power = 56 MW	2.82	3.56	3.93
EOL-MITR-DDE	End of Cycle 8 = EOL for MITR DDE			

The nominal average channel velocity of MITR DDE [Bert, 2022] s 2.6 m/s. The nominal channel velocity is the flow velocity at cross-section of fuel region where the flow area is 2213 mm^2. The frontal area of the inlet plenum duct in the CFD model is 6292.58 mm^2 according to the CAD model. The inlet velocity in the inlet plenum calculated by mass conservation to be 0.91434 m/s. The pressure outlet boundary is specified by 0 Pa gauge pressure, while the operating pressure is set at 1.2 MPa. The inlet temperature into the domain is considered to be 308.15K, whereas free convection boundary conditions are imposed in the outlet section of this domain.

2.3 MATERIAL PROPERTIES

The built-in IAPWS-IF97 water properties were adopted to specify the density, viscosity, thermal conductivity, specific heat, and dynamic viscosity of working fluid for both the RELAP5-3D and CFD models. IAPWS-IF97 is a temperature- and pressure-dependent water property. The temperature dependent density, specific heat, and thermal-conductivity for the U-10Mo fuel [Rabin et al., 2017] and Aluminum 6061 cladding [Polkinghorne & Lacy, 1991] are provided in Table 2. For the mechanical properties, Young's modulus and Poisson's ratio, no temperature or irradiation dependency is assumed. The values of these properties are taken as the one in the room-temperature, unirradiated configuration. No plastic deformations are expected and hence, only no plastic-deformation related properties are listed. Furthermore, the thermal diffusivity of the Zirconium liner between the fuel and the cladding is neglected.

Table 2. Thermophysical properties for fuel and cladding materials.

Material	Property	Equation	Temperature Validity Range
U-10Mo	Density [kg/m^3]	$\rho = -0.9215T[K] + 17409.0$	[293,623] K
	Specific Heat [J/(kg.K)]	$C_P = 0.0692T[K] + 113.61$	[293,623] K
	Thermal Conductivity [W/(m/K)]	$k = 0.0413T[K] + 0.1621$	[293,1073] K
	Young's Modulus [GPa]	88.4	-
	Poisson's Ratio	0.41	-

	[-]		
Aluminum 6061	Density [kg/m³]	$\rho = 2702.0$	[293,573] K
	Specific Heat [J/(kg.K)]	$C_P = 3.97 \times 10^{-5}T[K]^2 + 0.41T[K] + 773.0$	[298,805] K
	Thermal Conductivity [W/(m/K)]	$k = -1.73 \times 10^{-7}T[K]^3 + 2.66 \times 10^{-5}T[K]^2 + 0.16T[K] + 120.6$	[298,811] K
	Young's Modulus [GPa]	68.3	-
	Poisson's Ratio [-]	0.33	-

3. MODELS

The section summarizes the modeling approaches used for studying the thermal-hydraulics and mechanics fields. Thermal-hydraulics calculations are performed with RELAP5-3D (version 4.4.2) and STAR-CCM+ (version 16.06.101-R8). For validation of RELAP5-3D for this type of simulations we refer the reader to the references of this report [Miller & Shumway, 1992; Sloan et al., 1994; Weaver et al., 2002; Little, 2016; Maddock, 2017; RELAP5-3D, 2018; Narcisi et al., 2019; Collins, 2020; Martin & Williams, 2022]. Similarly, NQA-1 standard CFD modeling validation for this type of simulations for STAR-CCM+ can be bound in the provided references [Simcenter, 2020; Siemens, 2021; STAR-CCM+, 2021]. The mechanical calculations are performed with Abaqus 2021. ABAQUS quality assurance plan complies with the ISO 9001 and the ANSI/ASME NQA-1 quality assurance standards [Bryson & Dickson, 1993]. Details of the modeling approach implemented in each code are provided in the following subsections.

3.1   RELAP5-3D THERMAL-HYDRAULICS MODEL

The modeled flow geometry and configuration of the fuel plates in the MITR fuel assembly is presented in Figure 3. The modeled geometry consists of an inlet pipe with a fitting to the fuel array, the internal subchannel space between the plates of the array, and the outlet fitting and pipe. The flow bypasses in the fuel assembly are explicitly not modeled in the RELAP5-3D model. However, these flow bypasses are assumed to be 1% in the RELAP5-3D model and, hence, the inlet velocity is reduced by 1% to account for the effects of flow bypass. The fuel plates are divided in four transverse sections. Each of the sections is not explicitly modeled in the RELAP5-3D model as V4.4.2 of the software does not include the possibility of capturing heat conduction in this transverse direction. Therefore, only transversely average profiles are captured in the RELAP5-3D model. This assumption resulted in a difference in the predictions between RELAP5-3D and CFD.
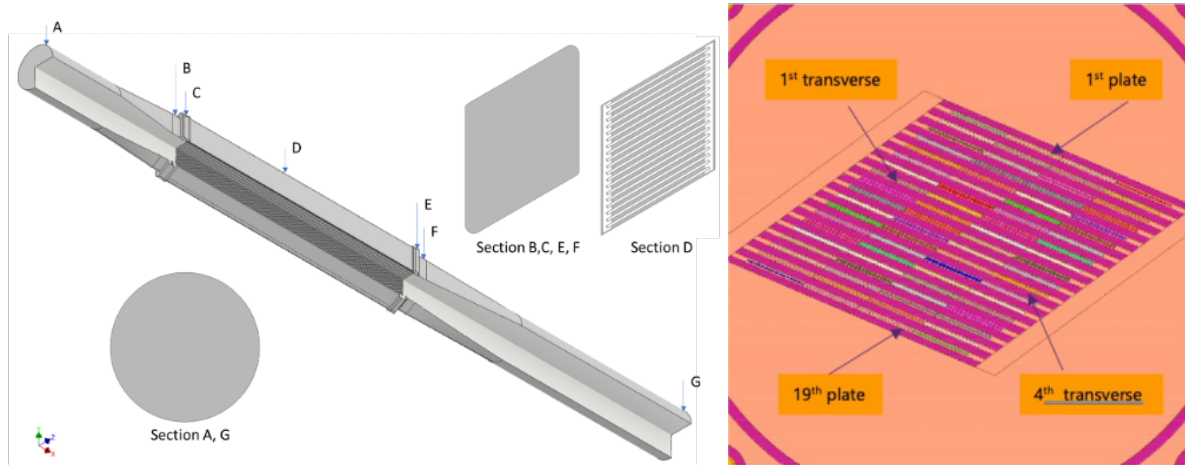
Figure 3. Left: modeled internal geometry for the fluid flow in the MITR test section. Right: Structure of the fuel plates in the MITR fuel assembly.
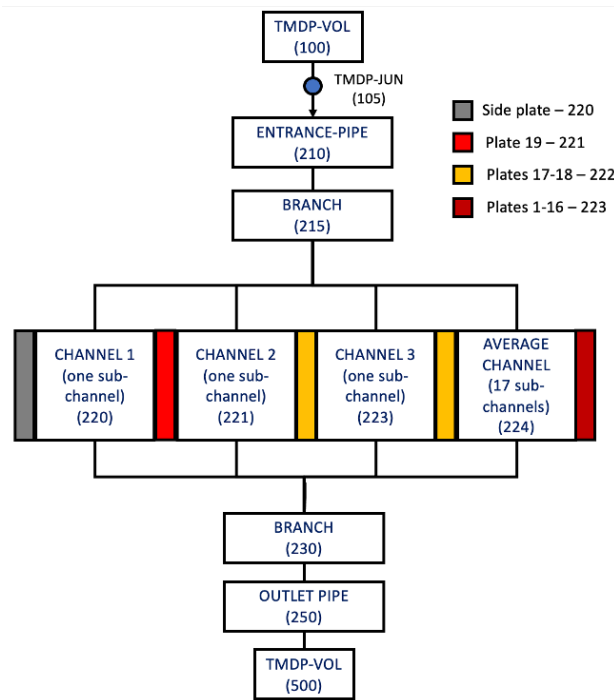

Figure 4. Nodal diagram for the RELAP5-3D MITR model.

The nodal diagram of the RELAP5-3D model is depicted in Figure 4. The inlet section to the fuel assembly is modeled via a pipe component of varying area and hydraulic diameter. The entrance fitting to the fuel assembly is modeled via a branch component. A four-channel configuration is used to model the fuel assembly. Channel 1 models the flow field between the side plate and fuel plate 19. Channel 2 models the subchannel between fuel plates 19 and 18 and channel 3 the one between fuel plates 18 and 17. Finally, channel 4 models an averaged sub-channel composed by remnant 16 internal flow channels plus the one between the side plate and fuel plate 1. Following static scaling principles, the flow rate and flow area in channel 4 are the sum of those channels composing channel-4 and the hydraulic diameter is the unweighted average of these ones. The flow geometry is closed with a branch component capturing the outlet fitting of the fuel assembly and the outlet pipe of varying hydraulic diameter.

Fuel plates 17, 18, and 19 are modeled via a flow-perpendicular and axially discretized heat structure. In the flow-perpendicular direction, the thickness of the fuel plate is captured. In this direction the fuel plate is composed by the external aluminum cladding and the U10Mo. The thickness of the U10Mo fuel varies depending on the type of plate as shown in Figure 2. The volumetric power is imposed directly in the U10Mo fuel without considering direct heating of the Aluminum cladding. The side plate is included in the model to capture the pressure drop due to the friction between the flow field and the fuel assembly basket. It is assumed that no nuclear power is being produced in this plate. Finally, plates 1 to 16 and the remaining side plate are lumped together into one heat structure. Note that the temperature fields obtained within this average heat structure will be unrealistic. However, since the integral power and flow rates are modeled in the average plate and sub-channel, respectively, the surface temperature will be the average obtained for plates 1-16. Hence, the surface temperature predicted in this average plate can be used to study oxide growth rates. The average plate is complemented with a symmetry boundary condition in the side of the plate not in thermal contact with the average cooling channel. Conjugated heat transfer is performed between fuel plates and the neighboring channels. For example, for plate 19, the left boundary condition will be provided by the temperature in channel 220 and the right one by the temperature in channel 221. The flow-parallel discretization of the plates is complemented with a cell left and right of the conjugated heat transfer boundaries. These cells are used to capture the oxide growth in the plate during irradiation. An initial oxide layer thickness of 2μm is assumed for each plate side boundary. Simulations are performed sequentially from BOC-1 to BOC-8 and the oxide thickness is updated at each irradiation cycle ending to capture the historic effects of oxide-driven thermal insulation in the plates during irradiation.

Two final remarks close the RELAP5-3D model description. First, for all cases, mesh sensitivity studies have been carried out to ensure that the axial discretization for channels and pipes. This ensures that the discretization used is fine enough not to cause changes in the hydraulic pressure drop under successive refinements. Second, we note that by default, RELAP5-3D uses the bulk temperature to compute the Fanning friction factor for the pressure drop. However, due to the large heat fluxes in the plates, we observed that the temperature of the coolant next to the walls can significantly differ from those in the bulk of the channels. Therefore, modifications have been made RELAP5-3D to enforce the usage of the predicted next-to-wall temperatures when computing the Fanning friction factor. This led to significantly better comparisons against the CFD simulations.

3.2   STAR-CCM+ CFD MODEL

A steady-state, Reynolds-Averaged Navier-Stokes (RANS) equation-based conjugate heat transfer (CHT) analysis was conducted for the CFD analyses. A fluid domain of CFD model was solved by adopting a segregated flow solver with a second order convection scheme, a segregated fluid temperature solver, adding gravity, and with the realizable $k - \epsilon$ model for the RANS closure. A two-layer model with all-y^+ was implemented for the near-wall two-layer wall treatment. The solid domain was solved by adopting the segregated solid energy solver. The inlet and outlet of MITR DDE were modeled with a velocity inlet boundary and the pressure outlet boundary, respectively. The power density is applied only at the fuel core. The oxide layer growth was modeled by the correlated Kim model [Kim et al., 2003; Kim et al., 2008]. The oxide layer was modeled as the thermal contact resistance between the cladding and coolant.

The simulation domain and mesh structure of MITR-DDE is depicted in Figure 5. The computational mesh of MITR DDE CFD model was generated by adopting the polyhedral mesh type with the prism boundary layers (4 layers) for the fluid domain and the polyhedral mesh with a thin mesher (3 layes) for the solid domain. Total number of cell in the computational mesh is 57.72 million. The base mesh sizes for fluid domain and solid domain are 1.8 mm and 10.0 mm, respectively.
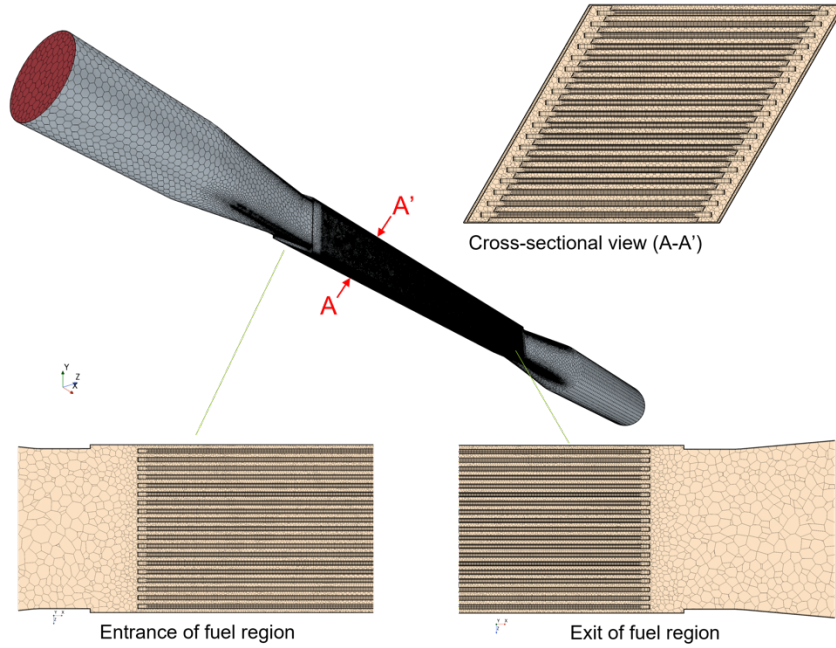
Figure 5. Domain geometry and mesh structure of MITR DDE CFD model.

A mesh independence study was performed to ensure the CFD mesh was sufficiently converged to accurately capture key quantities of interest (QOI). The results of this study are shown in Figure 6. The mass flow rate calculated based on given pressure drop across the MITR DDE was used as a QOI and the convergence study was performed. The mass flow rate changed by less than 4.8% across the whole domain for the finest mesh refinement giving confidence that the correct flow rate is captured. If it is assumed the convergence change is the uncertainty metric, then a three-sigma bound would by 14.4\% which is more than adequate for engineering uncertainties.

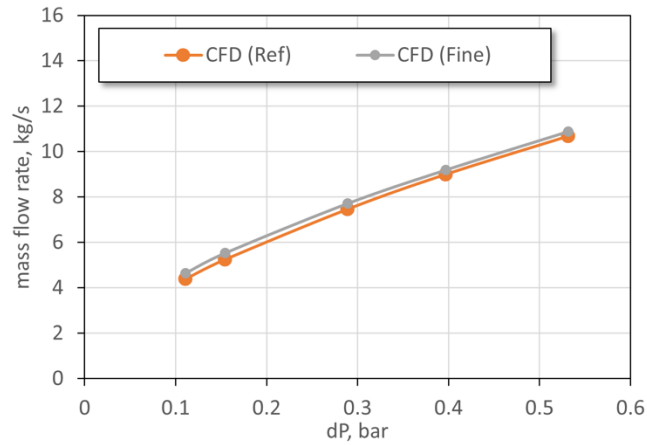Figure 6. Grid Convergence behavior for various pressure drop across the DDE.

3.3   ABAQUS MECHANICAL MODEL

The pressures on two sides of one plate would not be equal due to non-uniform flow distributions to the flow channels as well as the heating effect. Only deformation of the plate due to the pressure difference is evaluated in the ABAQUS calculation. Independent linear elastic deformation studies are

performed for each plate. Figure 7 shows the loads for the fuel assembly and boundary conditions per plate. Pressures are imposed perpendicular to each plate, while plates are clamped on their long edges. The pressure distributions on the cladding surfaces that are exported from the CFD calculation using a STAR-CCM+ table, and then imported to ABAQUS using a custom-developed Python script. The gravitational force is also considered in the Abaqus model.
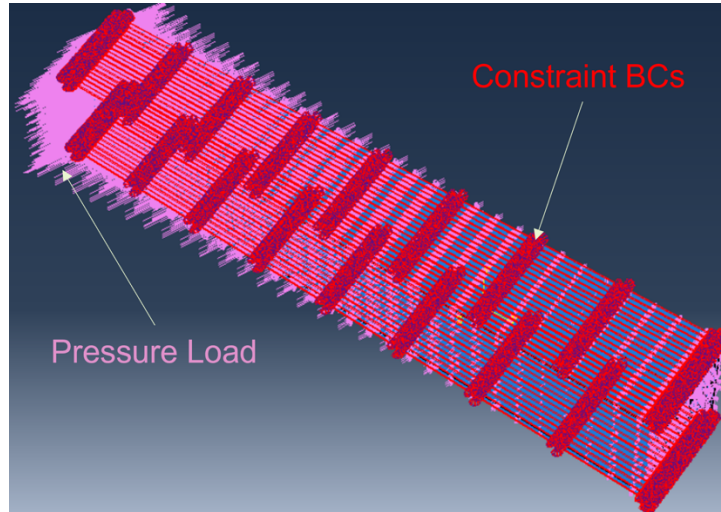

Figure 7. Pressure load and constraint boundary condition of ABAQUS model.

4. STUDY RESULTS

The present section summarizes key results of the study. At first, the velocity distribution over the channels and pressure drops predicted by the CFD and the RELAP5-3D model are compared for isothermal conditions. This exercise is used for cross verifying the CFD modeling conditions and gaining confidence in these ones. Then, the non-isothermal pressure-drop and velocity profile distributions are studied for all BOC configurations; from BOC-1 to BOC-8. Next, the oxide growth over the plates is studied for all BOC configurations. Finally, the deformations and stress distributions over the plates are analyzed.

4.1 COMPARING RELAP5-3D AND STAR-CCM+ RESULTS FOR ISOTHERMAL CONDITIONS

The exercise was performed for a hypothetical average channel velocity of 4.595 m/s. The goal of the exercise was to validate the CFD models against the more-widely-accepted RELAP5-3D ones. The transversally averaged axial pressure profile predicted by RELAP5-3D and the CFD model is compared in Figure 8. A good qualitative agreement is observed between both models. Logical differences are observed at the top and bottom fitting of the fuel array as the branch components in RELAP5-3D do not capture the full complexity of flow mixing in these regions. The total pressure drop predicted by CFD is 0.397 bar, whereas the one predicted with the RELAP5-3D model is 0.399 bar. The average flow velocity per channel and the percent error in the flow velocity predicted by RELAP5-3D and CFD are presented in Table 3 and Table 4, respectively. Flow velocities for channels 1 to 16 in the RELAP5-3D model is the same as all these channels are lamped together as presented in the nodal diagram in Figure 4. This is the reason why a larger difference is observed for the flow velocity between CFD and RELAP5-3D for channel 1 since the RELAP5-3D model does not explicitly capture this channel. The agreement, however, is much better for the equivalent side channel 20, which is explicitly resolved in the RELAP5-3D model. In general, a very good agreement is observed for the flow velocities predicted between both codes.

Finally, by analyzing Table 4, we remark a large difference between the average and maximum velocities predicted by CFD for each channel, evidencing a strong effect of the transversal flow distribution in the flow channels. We remark that the RELAP5-3D's lumped-parameters model is not able to capture the transversal flow dependency and hence, the transversal plate temperature computed with RELAP5-3D will be over-conservative when predicting oxide growth phenomena.
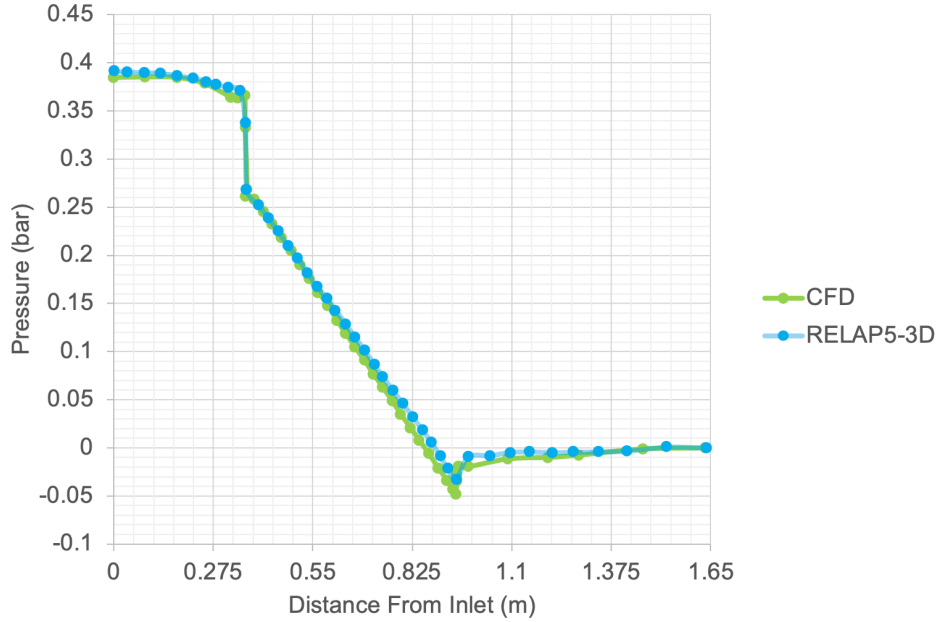

Figure 8. Comparison of isothermal pressure drop between RELAP5-3D and CFD models.

Table 3. Comparison of the velocity per channel between the RELAP5-3D and CFD models in isothermal conditions.

CH #	U_{mean} RELAP5-3D (m/s)	U_{mean} CFD (m/s)	U_{max} CFD (m/s)	CH #	U_{mean} RELAP5-3D (m/s)	U_{mean} CFD (m/s)	U_{max} CFD (m/s)
1	4.616	4.208	4.615	11	4.616	4.643	5.305
2	4.616	4.589	5.307	12	4.616	4.646	5.362
3	4.616	4.634	5.368	13	4.616	4.647	5.345
4	4.616	4.644	5.421	14	4.616	4.645	5.355
5	4.616	4.647	5.418	15	4.616	4.649	5.395
6	4.616	4.651	5.417	16	4.616	4.648	5.379
7	4.616	4.648	5.36	17	4.616	4.64	5.452
8	4.616	4.647	5.346	18	4.629	4.625	5.412
9	4.616	4.645	5.328	19	4.583	4.591	5.311
10	4.616	4.647	5.304	20	4.200	4.207	4.653

Table 4. Relative mean-squared percent difference between the RELAP5-3D and CFD models in isothermal conditions.

CH #	U_{mean} Difference CFD vs RELAP5-3D (m/s)	CH #	U_{mean} Difference CFD vs RELAP5-3D (m/s)
1	8.85%	11	-0.58%
2	0.59%	12	-0.64%
3	-0.38%	13	-0.66%
4	-0.60%	14	-0.62%
5	-0.66%	15	-0.71%
6	-0.75%	16	-0.69%
7	-0.69%	17	-0.58%
8	-0.66%	18	-0.09%
9	-0.62%	19	0.18%
10	-0.66%	20	0.16%

4.2   THERMAL-HYDRAULICS FIELDS FOR NON-ISOTHERMAL CONDITIONS

The total pressure drop and pressure profiles predicted with the RELAP5-3D and CFD models, respectively, is compared for all BOC configurations in Figure 9. The pressure profile is qualitatively similar to the isothermal one in Figure 8. Pressure drop is approximately negligible in the inlet pipe but much larger in the DDE channels. As approximately singular pressure drop (rise) is observed at the inlet (outlet) fitting of the fuel assembly due to the sudden flow acceleration into (deceleration out of) the fuel assembly. It is observed that the total pressure drop change ~1.5 kPa due to the difference in heating across the analyzed configurations. The largest difference in pressure drop is predicted between BOC-5 (colder) and BOC-6 (hotter) configurations. The hotter configurations present a reduction in pressure drop, due to the reduction in the flow viscosity. Nonetheless, the changes in pressure drop due to heating are only about 10% of the total pressure drop over the assembly and, hence, a second order effect in the pressure drop.
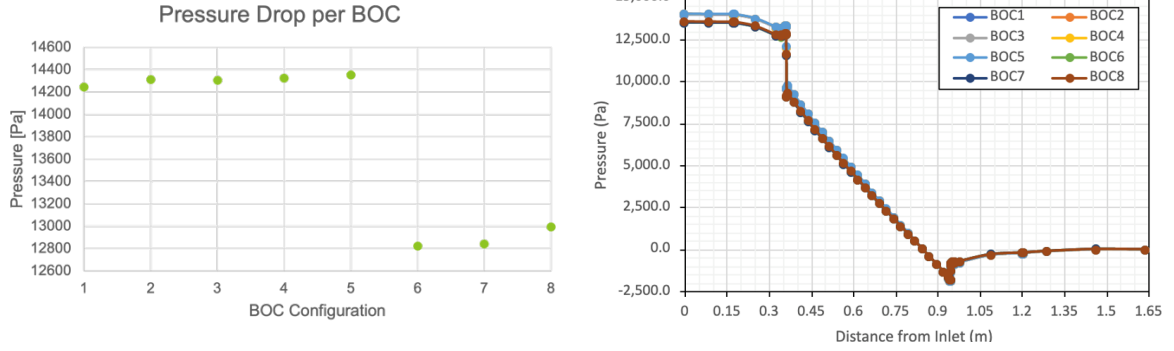
Figure 9. Left: total pressure drops predicted for all BOC configurations with the RELAP5-3D model. Right: pressure profiles predicted with the CFD model for all BOC configurations.

It is observed that the pressure drop increase from BOC-1 to BOC-5 due to the reduction in heating power and due to the shrinkage of the channels because of oxide growth; this latter effect is only captured in the RELAP5-3D model. Next, a sharp reduction in the total pressure drop is observed for BOC-6 as the heating power is increased. Finally, the pressure drop increase from BOC-6 to BOC-8 due to the reduction in the heating power and the shrinkage of the channels. The effect of the oxide growth on the pressure drop has been estimated to be ~0.1kPa. Hence, this effect is, at most, a third order effect in the pressure profiles. Therefore, these effects could be disregarded from the pressure drop when performing mechanical pressure drop studies for the MITR DDE.

Regarding the influence of heating in the pressure drop, two competing effects influence the pressure drop during flow heating. First, flow accelerates as density reduces due to heating, which will tend to increase the pressure drop. Second, viscosity reduces due to flow heating, which will lead to a reduction in the pressure drop. In these studies, the mass flow rate is constant. Since the fluid remains in liquid state, the density is almost constant. For instance, taking BOC-6 and BOC-1 as example cases, density reduces ~1.8% between inlet and outlet for BOC-6 and ~1.2% for BOC-1. However, the change in viscosity is more dramatic. Viscosity reduces ~51% between inlet and outlet for BOC-6 and ~32\% for BOC-1. This causes the average mass-length specific friction factor ($f/(\rho l)$) for BOC-6 (16010 N.s2/m5) to be about $9.4\% smaller than BOC-1 (17672 N-s2/m5). So, expressing the pressure drop via the Fanning friction factor (f) as $f\rho u^2/s$ and noting that ρu needs to be conserved since the mass flow is constant, we need to compare the product fu for evaluating the difference in pressure drop. However, we note also that $fu = f\dot{m}/(\rho A)$ and since the area (A) and mass flux ($\dot{m}$) is the same between the two configurations, this leads to the comparison of f/ρ for evaluating the differences in pressure drop. Taking BOC-1 as the reference, the numerator f reduces 9.4\% for BOC-6, and the denominator rho reduces only 0.6\%, which explains why the pressure drop for BOC-6 is smaller and, in general, why heating reduces the pressure drop.

CFD-calculated cross-sectional velocity distributions at the entrance, middle, and exit of the fuel region for the example BOC-6 are presented in Figure 10. By comparing the entrance and exit of the fuel region on can observed a non-negligible axial flow development through the channel.
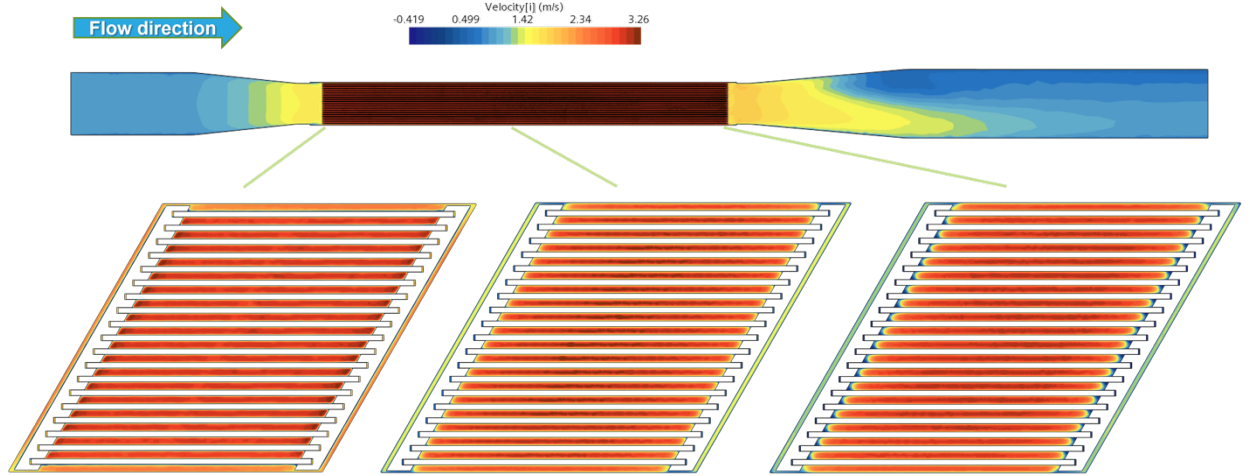
12

Figure 10. CFD-calculated cross-sectional velocity distributions at various locations.

Peak and surface-averaged channel velocities in the flow direction are depicted in Figure 11. The flow acceleration would affect the channel velocity; although, it is deemed that heating effect on the flow velocity distribution is not significant. Average channel velocities in the second irradiation campaign (BOC-6 to BOC-8) were slightly larger than those in the first campaign (BOC-1 to BOC-5) due to higher heating powers in the second campaign. However, the relative deviation of surface-averaged channel velocity between two campaigns is less than 1.05%. Hence, the effect of heating on peak channel velocity is deemed to be more negligible. Relative deviations of the peak channel velocity between two campaigns were less than 0.4%.
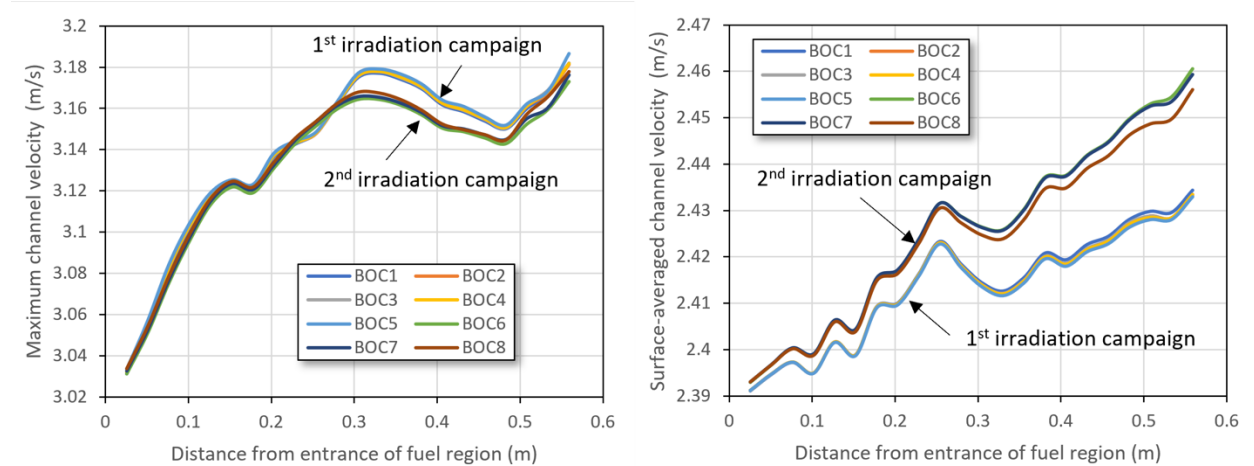

Figure 11. CFD-calculated channel velocity profiles (left: peak velocity, right: mean velocity).

In the CFD analysis, the bypass flow through the gaps between (i) the side plates and MUSTANG-R irradiation vehicle and (ii) between the fuel plates and side plates was modeled. To evaluate the amount of flow bypass, three sub-channels for the right and left bypass gaps and the flow channel were generated in the CFD model. The ratio of bypass flow to total flow is depicted in Figure 12. The bypass flow ratio at the entrance of the fuel region was 4.32% and it decreases to 2.8% as it flows to the downstream fuel region. The bypass flow would be a more significant factor affecting channel velocities. Decreasing

13

bypass flow results in increasing averaged and peak channel velocities. Due to the bypass flows, the average channel velocity was ~2.46 m/s which is slightly lower than the nominal velocity 2.6 m/s provided by SCK CEN.
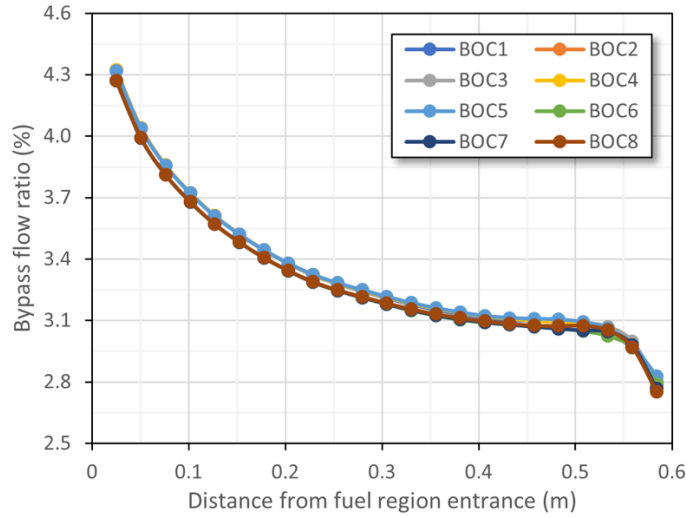

Figure 12. CFD-calculated channel velocity profiles (left: peak velocity, right: mean velocity).

The transversal-averaged coolant temperature profiles for all BOC configurations are presented in Figure 13. Since these results respond solely to enthalpic balance, only the RELAP5-3D results are computed. CFD results are equivalent within a tolerance of 0.1%. The temperature rise decreases from BOC-1 to BOC-5 as the heating power decreases. Then, it sharply increases due to the larger power in BOC-6 and then, decreases until BOC8 due to the reducing heating power. The thermal protective effects of the oxide growth layer do not play a significant role in the average temperature of the coolant. This is expected since the coolant average temperature rise should be determined by the enthalpy balance between the heat added into the flow and the temperature rise. The maximum temperature is of ~40K for
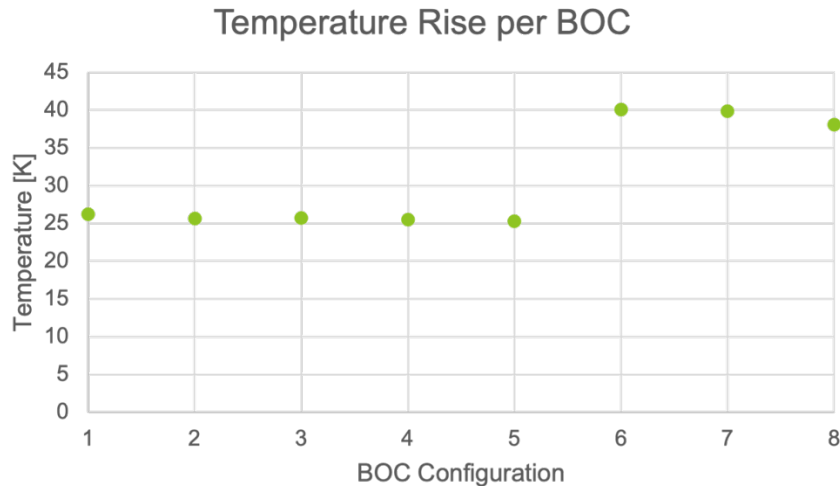
BOC-6.

Figure 13. Comparison of the total temperature rise over the full section for all BOC configurations for the RELAP5-3D models; CFD results are equivalent within 0.1% of tolerance.

CFD-calculated temperature distributions on the cladding surfaces and the peak temperatures of cladding and fuel core over the 19 plates for all BOC configurations are depicted in Figure 14. Although total heating power at BOC-6 was the largest during the campaign, the highest peak temperature was observed at BOC-7 due to the accumulated oxide layer thickness.
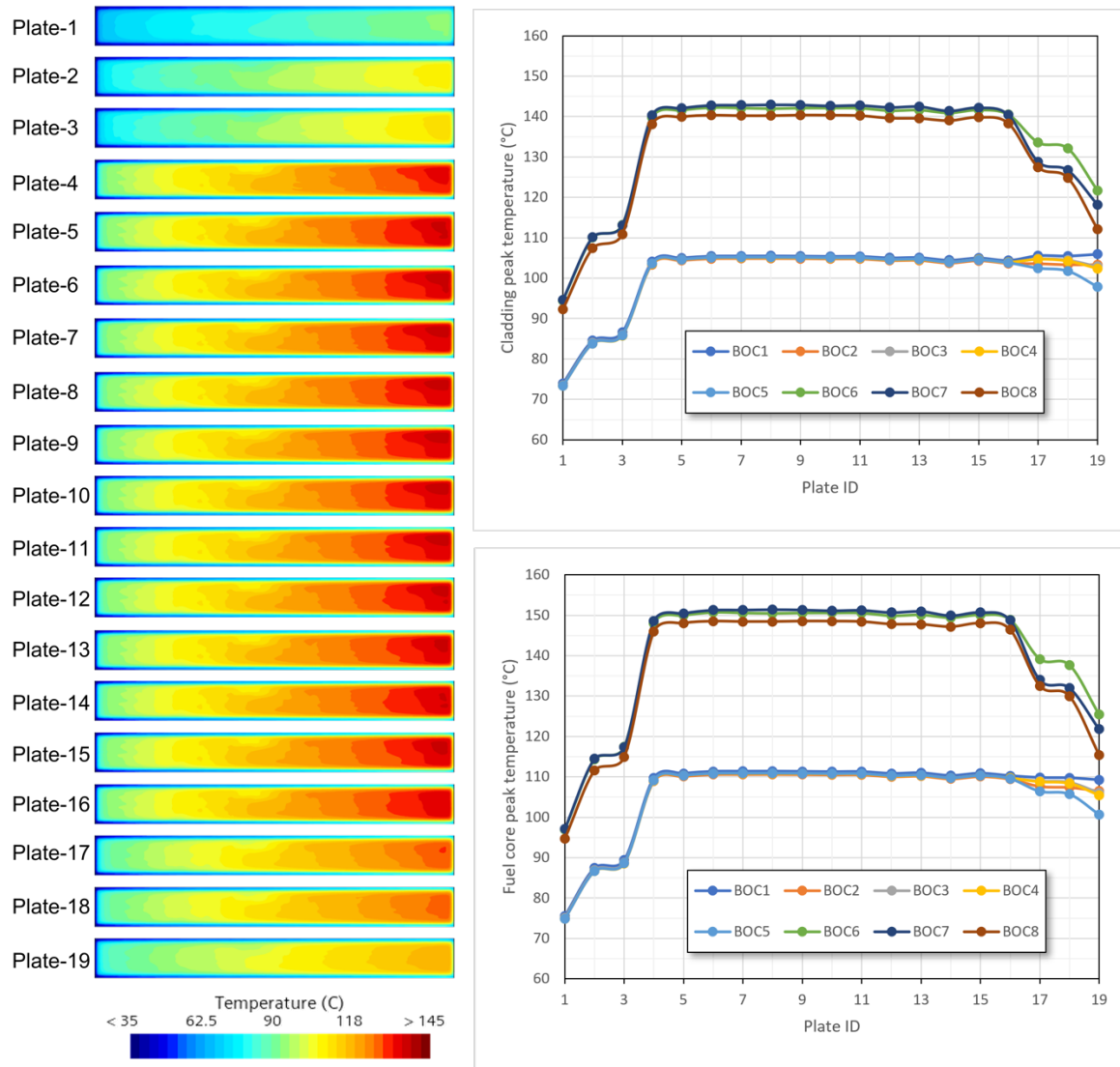

Figure 14. Left: Temperature distribution on the cladding surface for BOC6 (highest power configuration). Right: Peak temperature profiles (top: cladding, bottom: fuel core).

The influence of asymmetric power density can be found in Figure 15. Although the power density of plate 18 and plate 19 are larger than that of plates 1-16, the hottest plate in the MITR DDE was plate 8 because the thicknesses of fuel core of Type-Y (plate 18) and Type-T (plate 19) are thinner than that of Type-F (plates 4-16). Plate 1 and plate 19 are the same type of fuel plate (Type-T), but the two plates showed different peak temperatures due to different power densities. The peak fuel core and cladding temperature at BOC-7 are 151.42 °C and 142.92 °C, respectively.

The effect of power density variation during the campaigns is clearly shown in Figure 15. Decreasing power densities of plate 17-19 from BOC06 to BOC-8 during the second campaign led to decreasing temperatures of these plates. Peak temperatures calculated by the CFD were higher than the RELAP5-3D calculation result which is lumped value over the plate. For BOC-7, the peak temperature of the fuel core

calculated by the CFD was 25.57 K higher than that predicted by the RELAP5-3D, while the peak cladding temperature in CFD was 26.39 K higher than the one predicted by RELAP5-3D.
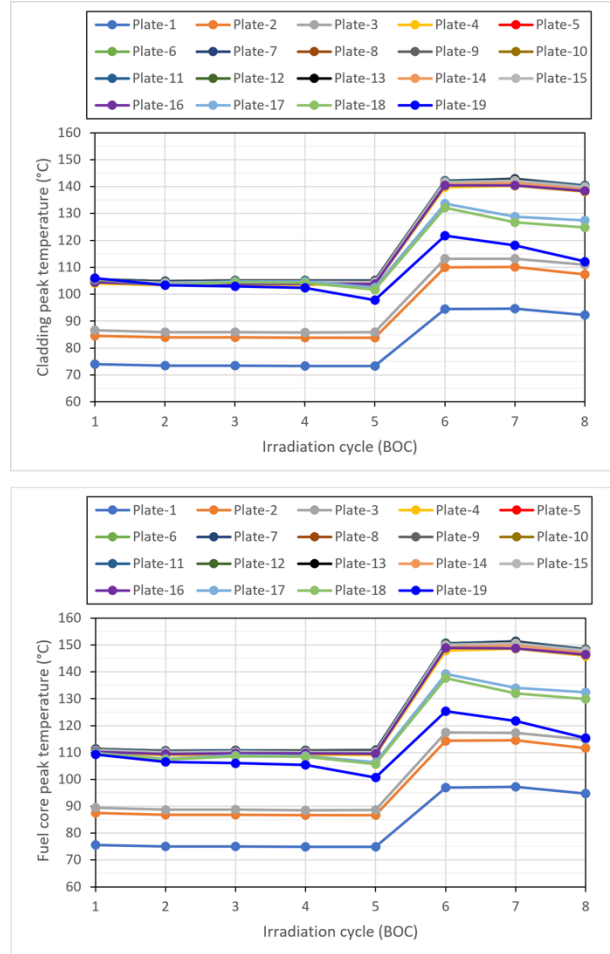

Figure 15. Peak temperatures as a function of irradiation cycle. (top: cladding, bottom: fuel core).

The heat transfer coefficient distributions of the plates depicted in Figure 16. In the CFD model, the inlet temperature (35 °C) is used as a reference temperature to calculate the heat transfer coefficient on the surface. The entrance of the fuel region is where the temperature difference between the plate and coolant is largest. Consequently, the value of the heat transfer coefficient at the entrance region was larger than that of the downstream region. Since the heat transfer coefficient depends on the differential temperature between the cladding surface and coolant, power densities of the plates affects the heat transfer coefficient.
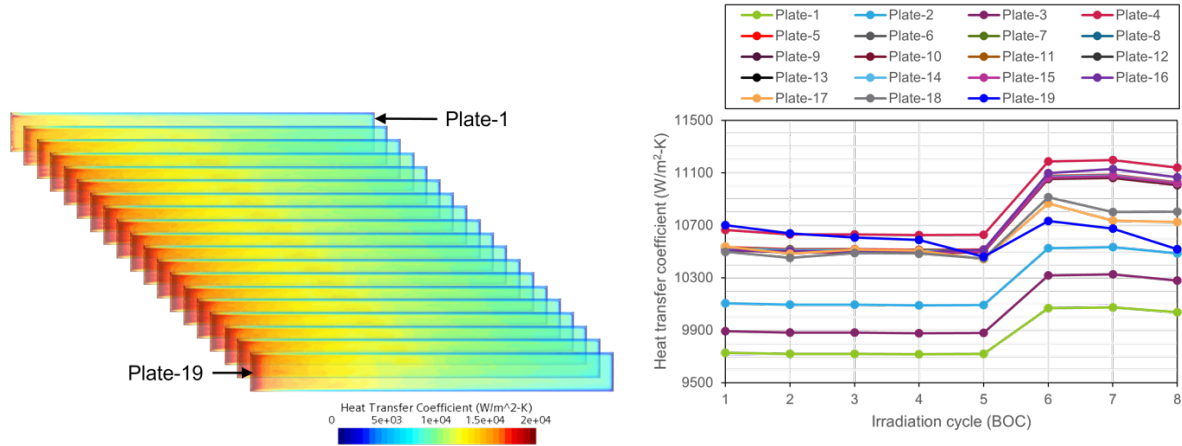
Figure 16. Left: heat transfer coefficient distribution on cladding surface for BOC6(largest power configuration). Right: heat transfer coefficient profile by the irradiation cycle.

4.3   OXIDE GROWTH STUDIES

The CFD model uses local fluid and fluid-solid interface temperatures and heat fluxes on the cladding surface to calculate the oxide layer thickness growth. Therefore, the CFD prediction for the oxide layer thickness is likely to be higher than that predicted by the RELAP5-3D. The CFD predictions for the oxide layer thickness distributions over the 19 plates for BOC-8 and for plate 8 over all BOC configurations is presented in Figure 17. The maximum oxide layer thickness formed on the plate 8 at the end of BOC08 was ~14.9 μm. Oxide layer thicknesses of the plates located on the side of the array, e.g., the plate 1 and plate 19, was formed relatively thin. Since the correlated Kim model uses the cladding temperature to calculate the value of exponent p, the oxide layer thickness is thick at high temperatures. Consequently, the oxide layer thickness distribution corresponds to the cladding temperature as shown in Figure 18.
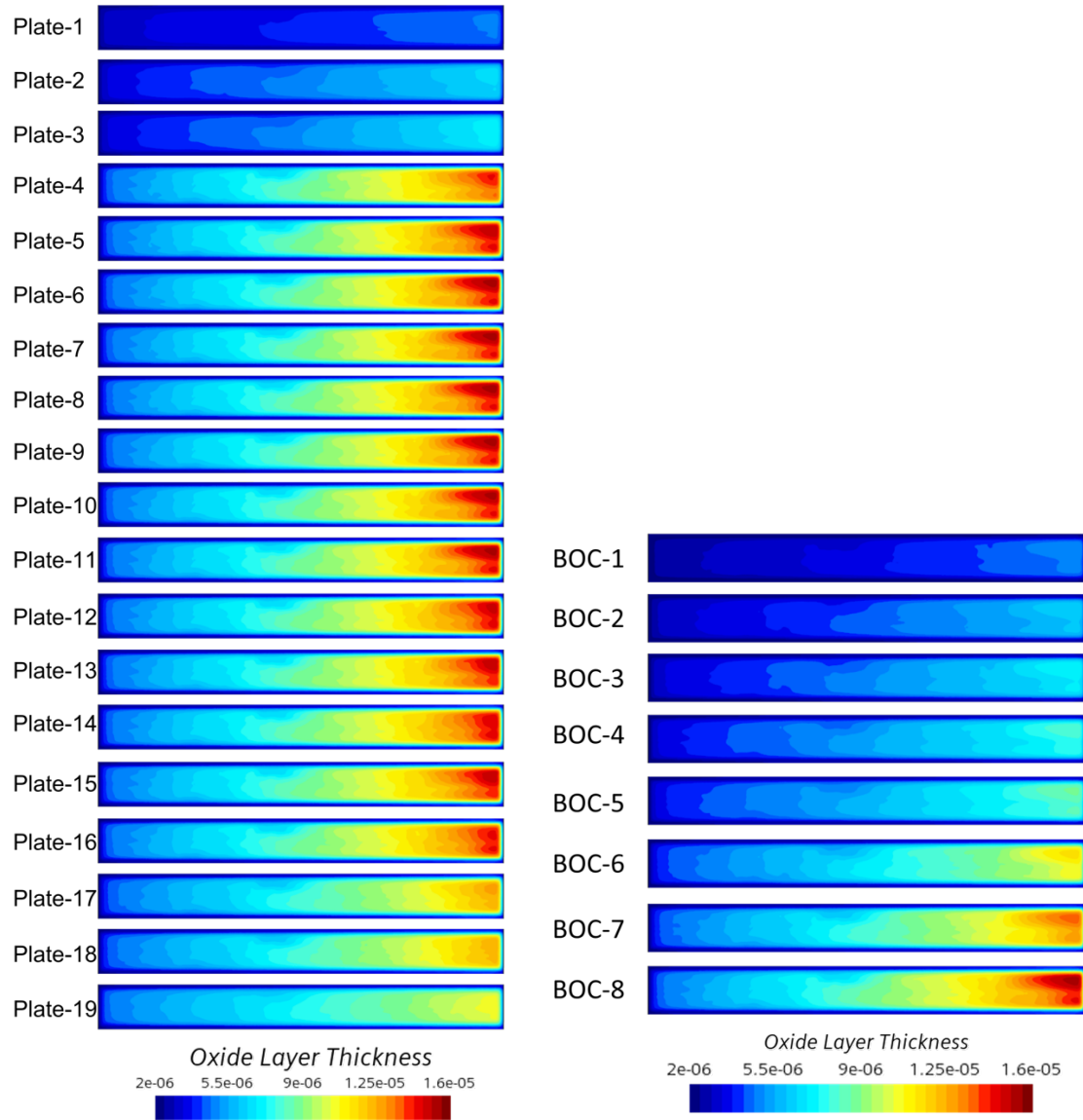
Figure 17. Left: CFD prediction for oxide layer thickness distributions over 19 plates for BOC-8 (last BOC configuration with largest oxide layers). Right: CFD prediction for the oxide layer growth on plate 8 (plate with largest oxide thickness) by BOC configurations.
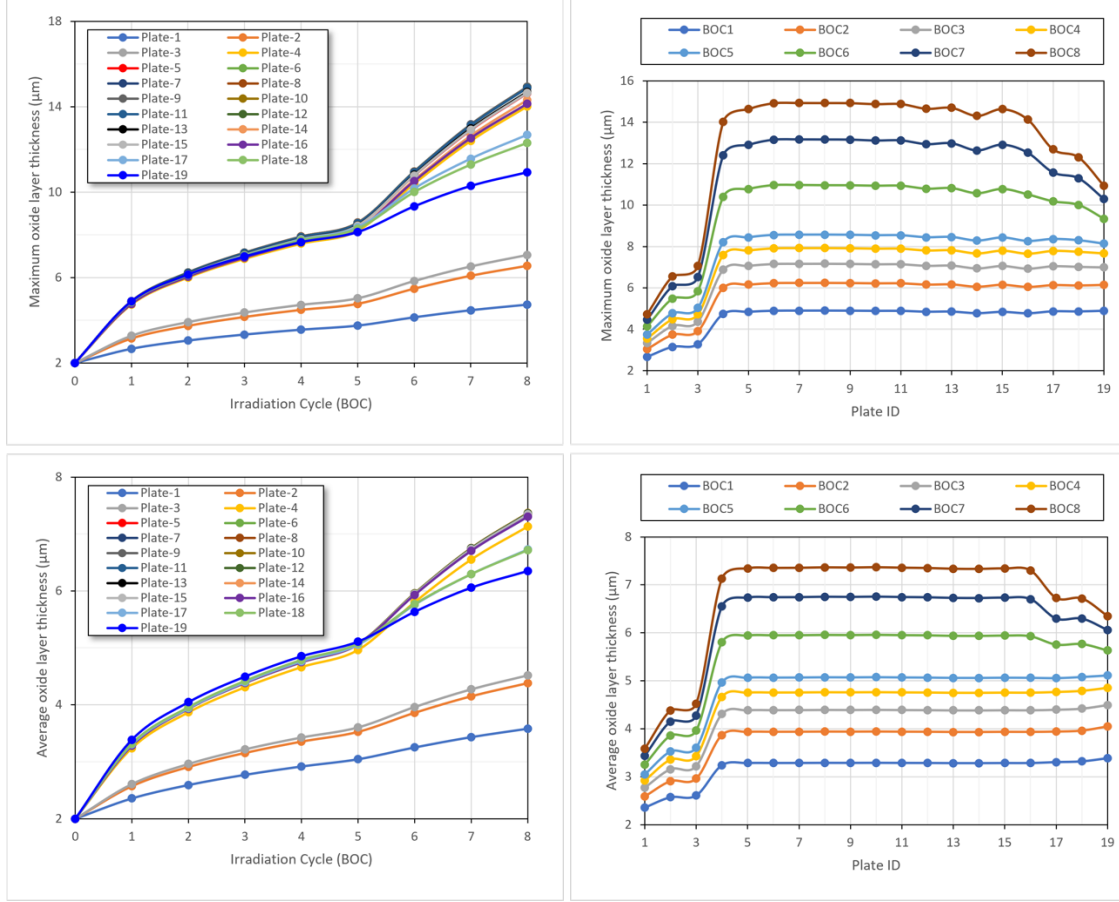
Figure 18. Left: CFD prediction for oxide layer thicknesses by BOC configuration (top: maximum thickness, bottom: surface-averaged thickness). Right: CFD prediction for oxide layer thickness profiles by the plates (top: maximum thickness, bottom: surface-averaged thickness).

4.4   STRUCTURAL ANALYSES

The left frame of Figure 19 shows pressure loads on the cladding surfaces imported into the ABAQUS model through analytical fields. The right frame of Figure 19 depicts the deformation and the stress distributions over 19 plates for BOC6. Maximum values of displacement and Von Mises stress are presented in Figure 20. Maximum deformation of the plate is expected to be ~3 μm during the normal operation cycles. The maximum stress value over all irradiation campaigns was less than 0.86 MPa, which is much smaller than the minimum yield stress in transverse direction at room-temperature conditions (274 MPa). Note that these results may be different if temperature-dependent mechanical properties are considered for the plate.
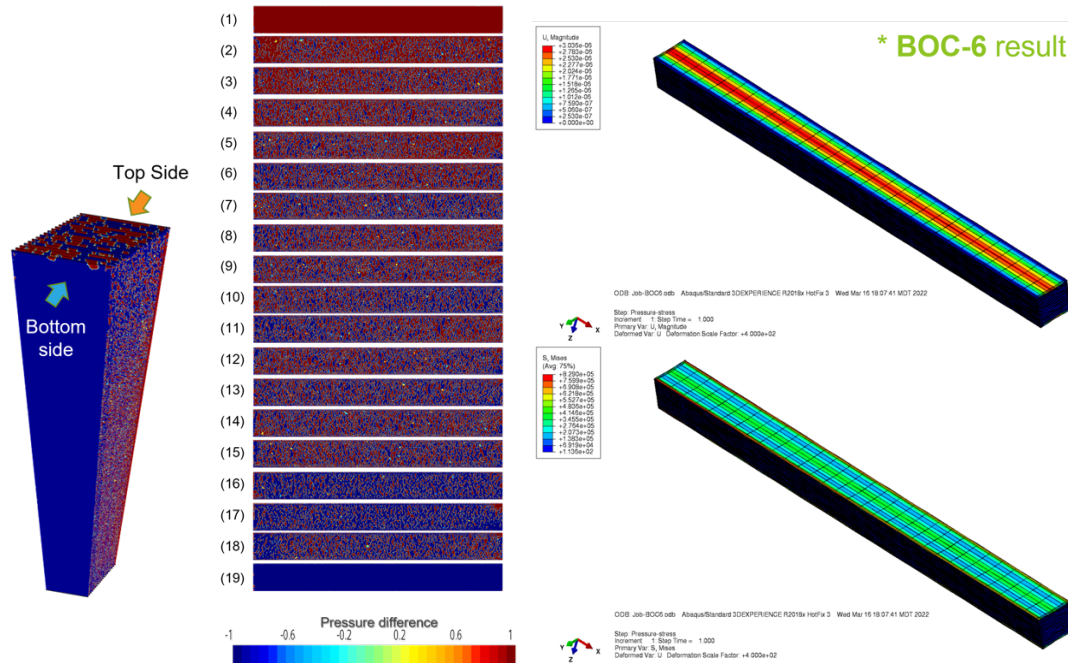
Figure 19. Left: Distribution of pressures over the fuel plates for BOC-6. Right: ABAQUS calculation results for BOC6 (top: plate displacement, bottom: Von Mises stress).
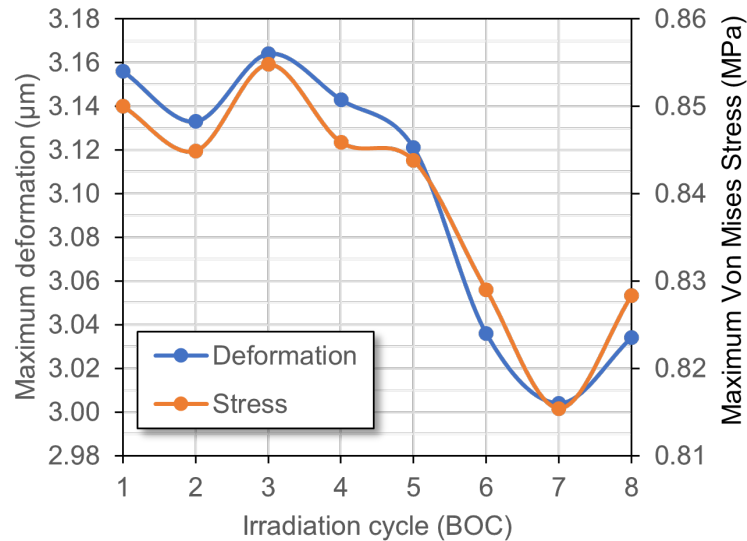

Figure 20. Maximum displacement and Vol Mises Stress at different BOC configurations.

Higher flow rates could increase hydrodynamic pressure induced plate deformation and stress. To assess the plate deformation and structural stress at high mass flow rate, STAR-CCM+ and ABAQUS calculations were conducted for the mass flow rate of 22.645 kg/s which corresponds to 1.8 bar pressure drop across the MITR DDE. The calculation results are presented in Figure 21. The maximum deformation and Von Mises stress of the MITR DDE were 24.56 μm and 6.63 MPa, respectively. These maximum values were observed on most outer plates (plates 1 and plate 19). The plate deformation on

interior plates was less than 1 μm. The Von Mises stresses on the interior plates were also small. Therefore, this calculation confirms that the impact of hydrodynamic pressure on the plate structural integrity is negligible when considered the normal pressure loads at both sides of the plates.
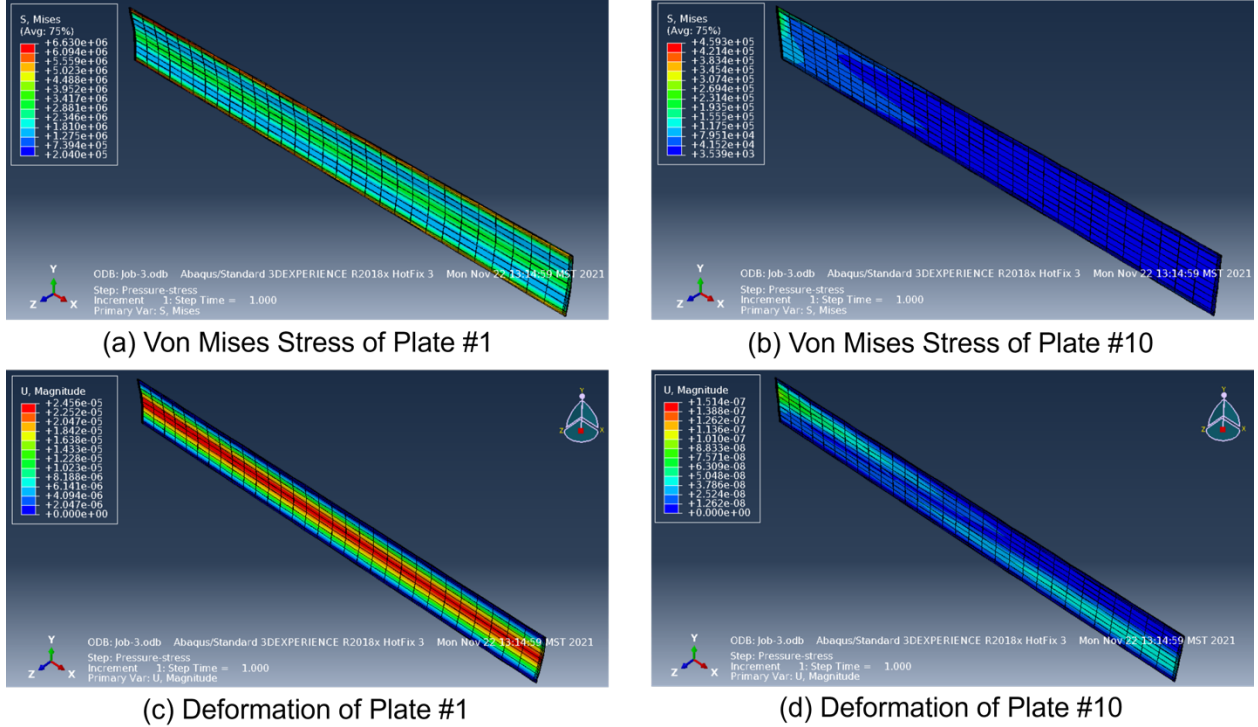

(a) Von Mises Stress of Plate #1

(b) Von Mises Stress of Plate #10

(c) Deformation of Plate #1

(d) Deformation of Plate #10

Figure 21. ABAQUS calculation results with postulated high mass flow rate of 22.645 kg/s.}

5. CONCLUSIONS

In this report, the thermal-hydraulic calculations using the system thermal-hydraulic code RELAP5-3D, the CFD code STAR-CCM+, and the mechanical analysis using FEA code Abaqus were conducted to support the performance analysis of MITR DDE for two irradiation campaigns. Key findings are:

- RELAP5-3D and CFD predictions for the pressure drop over the whole test section (inlet pipe, fuel assembly, and outlet pipe) agreed well with each other (maximum differences ~5 \%). This indicates that both RELAP5-3D and CFD could be used for performing studies of pressure drops for different flow rates. However, RELAP5-3D friction models must be adjusted to explicitly use near-wall temperatures for computing the skin friction coefficients as the code uses bulk temperature by default leading to over-estimated pressure drops.

- Transverse-averaged temperature over the fuel plates agree very well between RELAP5-3D and CFD analyses. The maximum averaged temperature rises for the coolant in the fuel plates was ~ 40 K for BOC6, whereas the minimum was ~25 K for BOC5. However, larger differences have been obtained in the peak cladding and fuel core temperatures as RELAP5-3D does not capture transversal temperature variations. We therefore recommend performing the computations of the maximum cladding and fuel core temperatures using CFD as RELAP5-3D results can be under-conservative.

- In CFD, the bypass flow through the gaps between the side plate and MUSTANG-R irradiation vehicle, and between the fuel plates and side plates were 4.32% of total flow rate at the entrance of the fuel region and reduced by 2.8% at the exit of the fuel region.

- The CFD with the correlated Kim Model predicted that the maximum thickness of the oxide layer would be 32.24 μm at the end of BOC-8. The CFD prediction was much greater than the RELAP5-3D prediction which is less than 4 μm. The lumped modeling approach of RELAP5-3D would underestimate the maximum oxide layer thickness. Further investigation and validation for the oxide layer growth models are needed

- Abaqus analysis results showed that hydrodynamic pressure-induced plate deformation and structural stress are negligible when regarding the pressure drop and flow distribution over the test section.

6. REFERENCE

Bryson, J. W., & Dickson, T. L. (1993). *Stress-intensity-factor influence coefficients for axial and circumferential flaws in reactor pressure vessels* (No. CONF-930702--4). Oak Ridge National Lab.

A. Collins, "VTR modeling and simulation using INL RELAP5 system code, ECAR-4788, 2020.

B. Rabin, M. Meyer, J. Cole, I. Glagolenko, G. Hofman, W. Jones, J. Jue, D. Keiser Jr, Y. Kim,C. Miller,et al., "Preliminary report on u-mo monolithic fuel for research reactors,"Idaho NationalLaboratory INL/EXT-17-40975, 2017.

B. Rossaert, "Briddes-mustang-r critical velocity analysis for mitr and nsbr, calculation note-nc4986/n0brid-des/02/br,"Restricted Contract Report SCK CEN/46944057 (R-8944), 2022.

C. MIller and R. Shumway, "Relap5/mod3 code quality assurance plan for ornl ans narrow channelflow and heat transfer correlations," EG and G Idaho, Inc., Idaho Falls, ID (United States), Tech.Rep., 1992.

C. Xing, "Thermal Performance of the AFIP-7 Fuel Assembly in the ATR Center Flux Trap,"ECAR-4741, 2019.

J. C. Griess, H. C. Savage, and J. L. English, "Effect of heat flux on the corrosion of aluminum bywater. part iv. tests relative to the advanced test reactor and correlation with previous results,"ORNL-3541, 1964. DOI:10.2172/4077613. [Online]. Available:https://www.osti.gov/biblio/4077613.

R. E. Pawel, "On the kinetics of the aluminum-water reaction during exposure in high-heat flux testloops: 1, a computer program for oxidation calculations,"ORNL/TM-10602, 1988. DOI:10.2172/5524442. [Online]. Available:https://www.osti.gov/biblio/5524442.

R. Little, "Results of Physics Calculations in Support of RELAP5 analysis of the enhanced LEU fuel(ELF) MK 1A,"ECAR-2469, 2016.

R. Martin and J. Williams, "Safety software evidence ranking for determining analytical readinesswith a case study utilizing relap5-3d," inThe 19th International Topical Meeting on Nuclear ReactorThermal Hydraulics (NURETH-19), Mar. 2022.

RELAP5-3D Code Development Team, "Relap5-3d code manual. volume 4, models and correla-tions," Idaho National Laboratory, Tech. Rep., 2018.

Release notes for relap5-3d version 4.4.2.2021. [Online]. Available:https://relap53d.inl.gov/Shared%5C%20Documents/Release%5C%20Notes/Release%5C%20Notes%5C%20for%5C%20RELAP5%5C%204.4.2.pdf.

S. J. Pawel, D. K. Felde, and R. Pawer, "Influence of coolant ph on corrosion of 6061 aluminumunder reactor heat transfer conditions,"ORNL/TM-13083, 1995. DOI:10.2172/205846. [Online].Available:https://digital.library.unt.edu/ark:/67531/metadc671895.

S. Polkinghorne and J. Lacy, "Thermophysical and Mechanical Properties of ATR Core Materials,"EG&G Idaho Inc., Internal Technical Report, 1991.

S. Sloan, R. Schultz, and G. Wilson, "Relap5/mod3 code manual," EG and G Idaho, Inc., Idaho Falls,ID (United States). Idaho National ..., Tech. Rep., 1994

S. Kalcheva, "Feasibility study for dde-mitr and nbsr irradiation in br2 november 2021 – ed01,"SCKCEN, Document BR2-RCE-RFA, Table XIX (MITR DDE) and XX (NBSR DDE), 2021.

Siemens Digital Industries Software,STAR-CCM+ User Guide 2022.1.1, 2021.

Simcenter star-ccm+ verification suite, 2020.

STAR-CCM+ Software Completes ASME NQA-1 Compliance Press Release, 2021. [Online].Available:https://www.plm.automation.siemens.com/global/en/our-story/newsroom/siemens-press-release/43868.

T. L. Maddock, "Results of Physics Calculations in Support of RELAP5 analysis of the enhancedLEU fuel (ELF) design,"ECAR-2230, 2017.

Thermal Performance of the FUTURE-HFIR fuel plates in the BR2 reactor, ECAR-5107,2019.

V. Narcisi, P. Lorusso, F. Giannetti, A. Alfonsi, and G. Caruso, "Uncertainty quantification method forrelap5-3d© using raven and application on nacie experiments,"Annals of Nuclear Energy, vol. 127,pp. 419–432, 2019.

W. L. Weaver, E. Tomlinson, and D. Aumiller, "A generic semi-implicit coupling methodology for usein relap5-3d©,"Nuclear Engineering and Design, vol. 211, no. 1, pp. 13–26, 2002.

Y. S. Kim, G. Hofman, A. Robinson, J. Snelgrove, and N. Hanan, "Oxidation of aluminum alloycladding for research and test reactor fuel,"Journal of Nuclear Materials, vol. 378, no. 2, pp. 220–228, 2008, ISSN: 0022-3115. DOI:https://doi.org/10.1016/j.jnucmat.2008.06.032. [Online].Available:https://www.sciencedirect.com/science/article/pii/S0022311508003590.

Y. S. Kim, G. L. Hofman, N. A. Hanan, and J. L. Snelgrove, "Prediction model for oxide thickness onaluminum alloy cladding during irradiation," in2003 International Meeting on Reduced Enrichmentfor Research and Test Reactors (RERTR), Chicago, IL, Oct. 2003.